

## The transition from density-driven to wave-dominated isolated flows

By RICHARD MANASSEH<sup>1</sup>†, CHANG-YUN CHING<sup>2</sup>  
AND HARINDRA J. S. FERNANDO<sup>2</sup>

<sup>1</sup>School of Mathematics, Fluid Dynamics Group, University of New South Wales,  
Sydney, NSW 2052, Australia

<sup>2</sup>Environmental Fluid Dynamics Program, Department of Mechanical and Aerospace Engineering,  
Arizona State University, Tempe, Arizona 85287, USA

(Received 1 June 1995 and in revised form 5 December 1997)

An isolated fluid mass travelling horizontally in a stratified layer is a phenomenon described alternatively as a detached gravity-current head or a strongly nonlinear solitary wave. A key feature of this flow is the transport of mass. Laboratory experiments examine the transition in time from a regime in which the flow is density driven, to one in which it is wave dominated. A simple means of creating this transitional regime, an isolated flow that exhibits both density and wave effects, is achieved by dropping a thermal into a linearly stratified layer. This transitional regime is called an 'isolated propagating flow'. Parameters for which the transitional regime occurs are identified. Particle-tracking studies reveal the vertical flow structure. There is an upper zone that is wave dynamical, and a lower zone in which transport of mass occurs. The transported mass slowly leaks out, until the phenomenon resembles a weakly nonlinear solitary wave. The experiments mimic a thunderstorm microburst impacting a temperature inversion, which has aviation safety implications. In the ocean, cracks in the ice cap (polar leads) cause similar flows impacting the thermocline.

---

### 1. Introduction

Gravity currents are density-driven phenomena that transport mass as a first-order effect. Solitary waves, like other fluid waves, transport momentum and energy. They travel unchanged in shape and form owing to a balance between nonlinearity and wave dispersion. However, weakly nonlinear solitary waves do not transport mass over long distances.

This paper is a study of an isolated propagating flow. Such disturbances are a transitional regime between a density-driven current propagating in a stratified layer and a weakly nonlinear solitary wave. They occur as initially density-driven flow that evolves with time into wave-dominated flow. They create strong, oscillatory flow patterns in a medium that supports waves. They transport mass like a density-driven current, violating some precepts of wave mechanics. However, unlike the current, there is no upstream source of dense fluid driving the flow. Hitherto, such phenomena have been described either as detached gravity-current heads or as solitary waves. It could be argued that they are intensely nonlinear solitary waves. However, for

† Current affiliation: Advanced Fluid Dynamics Laboratory, CSIRO DBCE, PO Box 56, Highett, VIC 3190, Melbourne, Australia.

the purposes of this paper a special terminology has been adopted to stress that neither description is wholly adequate. We base our definitions on the degree to which mass is transported. Thus *wave-dominated* behaviour is defined as a regime where mass transport has ceased. This is provided, of course, that other characteristics of wave-like behaviour (such as propagating oscillatory velocity and pressure fields) are present.

### 1.1. Gravity currents in stratified fluids

Much of the substantial body of research on gravity (or density) currents and related phenomena is summarized in the book by Simpson (1987). A gravity current is inherently a strongly nonlinear phenomenon that transports mass; unlike a solitary wave, it cannot be described using a weakly nonlinear correction to a linear solution. It has a well-known structure consisting of a raised head and a following flow. Within the head, near the bottom surface there is a feeder current that moves faster than the gravity-current propagation speed, and brings fluid to the top of the head. Thus there is a flow of transported mass through the head.

Gravity currents have been described by hydraulic theory (Benjamin 1968). A special case of a gravity current is relevant to the present paper: it is a gravity current propagating into a stably stratified layer. When a region of mixed fluid collapses into a stratified layer, a gravity current is formed if the height of the mixed-fluid region is considerably larger than the layer depth (Britter & Simpson 1981). If the mixed-fluid region is not so large, solitary waves may form (Maxworthy 1980). Under some circumstances, the head of the gravity current may detach from the following flow and travel ahead as an isolated 'blob' of fluid (Maxworthy 1980), having a similar appearance to a solitary wave. The leading portion of the following flow may then develop a new head which can subsequently detach as well (Simpson 1987). Whenever a head 'detaches', however, there is always a thin trail of dense fluid leaking out behind it. Numerical calculations by Hasse & Smith (1989) showed that a gravity current propagating into a stable layer could spawn from its head a solitary-wave-like disturbance with closed circulation.

### 1.2. Solitary waves in stratified fluids

Considerable research has been done on solitary waves in stratified fluids. Long (1953) presented an integral of the momentum equation along a streamline in a form appropriate to stratified fluids, which has been used in much subsequent analysis. Solitary waves in deep fluids containing a thin stratified layer were first treated analytically by Benjamin (1967) and independently by Davis & Acrivos (1967) and Ono (1975). An equation, usually called the Benjamin–Davis–Ono (BDO) equation after its discoverers, can be derived for a system in which weak nonlinearity balances wave dispersion. The BDO equation is for the horizontal wave structure and admits soliton solutions. The BDO equation is appropriate to an upper boundary condition of an infinite neutrally stratified layer overlying the pycnocline. If a 'rigid lid' tops the pycnocline, the Korteweg–de Vries (KdV) equation is the appropriate formulation.

Numerical work reported by Davis & Acrivos (1967) was based on Long's equation, as was more recent numerical work by Tung, Chan & Kubota (1982), extended by Brown & Christie (1994). These calculations show a topological change in the vertical structure once the amplitude becomes large relative to the thickness of the stratified layer. A recirculation zone or region of closed streamline flow forms, which must contain mass transported with the wave. This invalidates the principle of a

continuous streamline with known upstream conditions, on which Long's equation and the calculations are based.

Davis & Acrivos (1967) also showed experimentally that 'lumps' of fluid appeared to travel with the wave propagation velocity and regions of closed streamline flow were often observed. Since then, several authors (notably Stamp & Jacka 1995) have observed similar phenomena, where mass appears to be transported with the solitary wave. Stamp & Jacka (1995) studied solitons on a thin density interface. They observed counter-rotating cells which were not true closed-streamline regions, with fluid continually being entrained into and ejected from the cells. No other investigations of the vertical structure within the wave have been reported, though in experiments referred to above, transported mass was reported to appear turbulent.

The observed speeds of solitary waves have generally agreed with numerical solutions to Long's equation. However, the vertical structure of the wave, incorporating the mass-transporting recirculation zone, is hard to predict. This vertical structure is likely to be of great practical importance to flows in the environment.

### 1.3. Environmental evidence for a transitional regime

There are atmospheric and oceanic applications where wave-like disturbances transporting mass play an important role. There may also be geological situations within the Earth where these phenomena are important: solitary disturbances transporting mass are thought to be relevant to physics in the Earth's mantle (Grimshaw, Helfrich & Whitelaw 1992). In the ocean, polar 'leads' are thin, long cracks caused by plastic failure of the ice cap. In the winter, the exposed water re-freezes immediately, generating plumes and thermals of increased-salinity water. These may generate disturbances transporting mass on impacting a thermocline below (Noh, Fernando & Ching 1992).

Among the atmospheric phenomena is the gust front created in a stratified atmosphere (a low-level temperature inversion) by a thunderstorm outflow. Relevant observations and analyses include those of Shreffler & Binkowski (1981), Fulton, Zrnić & Doviak (1990), Doviak & Ge (1984), Doviak, Chen & Christie (1991) and Manasseh & Middleton (1995). These disturbances are thought to be a hazard to aircraft because they transport unpredictable wind shear far from the original thunderstorm outflow (Doviak & Christie 1989). A pilot negotiating the disturbance should understand its vertical structure in particular.

Comparisons with weakly nonlinear wave theory work best for large-scale atmospheric disturbances, not thunderstorm phenomena. An example is the mesoscale 'Morning Glory' of northern Australia (Clarke, Smith & Reid 1981; Haase & Smith 1984; Christie 1992; Alpers & Stilke 1996). However, even in these cases, a wave amplitude must often be chosen that probably renders the weak nonlinear assumption invalid. This makes successful results possibly fortuitous (Rottman & Einaudi 1993).

In general, weakly nonlinear wave theory has been used with some success, albeit with decreasing mathematical validity, for amplitudes up to about half the stratified layer thickness. Usually the wave speed can be well matched by weakly nonlinear theory, but the structure is poorly predicted (Noonan & Smith 1985; Manasseh & Middleton 1995). Supporting these observational findings, the experiments of Stamp & Jacka (1995) found the wavelength-amplitude relationship predicted by weakly nonlinear theory broke down at larger amplitudes. Analytic and numerical work that permits full nonlinearity, subject to a constant-vorticity assumption, shows that the streamline structure alters greatly as amplitude increases (Pullin & Grimshaw 1988; Forbes & Belward 1996; Evans & Ford 1996).

Laboratory realizations of the scenario in which gravity currents engender solitary

waves are given by the experiments of Rottman & Simpson (1989). Laboratory thermals hitting a density interface – a situation which models polar leads and perhaps also thunderstorm events – were shown to generate solitary waves by Noh *et al.* (1992).

To summarize §1.1–§1.3, there exist conceptual and analytical tools based on hydraulics used to treat density-driven currents (e.g. Benjamin 1968), and tools based on wave mechanics that are useful for describing solitary waves (e.g. Benjamin 1967). These models have separate theoretical bases that do not overlap. However, it appears that nature can produce a hybrid: an isolated propagating flow, which appears during the transition in time from density-driven to wave-dominated flow.

In the present experiments, the use of a thermal to create the disturbance is thought to be a natural way of generating an isolated propagating flow. The thermals and isolated propagating flows were chosen to be two-dimensional. The isolated propagating flows are to be created in a linearly stratified layer immediately overlying a solid boundary. This has the advantage of being a system for which an analytical solution under linear and weakly nonlinear theory is available.

The experiments are also an analogue of a linear thunderstorm microburst impacting a temperature inversion overlying the ground. (Many microbursts are axisymmetric in form, and hence evolve differently to the ones studied here. However, linear microbursts also occur, formed by several axisymmetric microbursts along a line. These are thought to pose a greater aviation hazard than individual axisymmetric microbursts (Hjelmfelt 1988).)

The paper is organized as follows. Section 2 explains the experiment. Section 3.1 outlines an appropriate weakly nonlinear theory for solitary waves, §3.2 describes methods of summarizing the results non-dimensionally. Section 4 describes the results and in §5 some discussion of the significance of the results is presented.

## 2. Experimental system and method

A Perspex tank of dimensions  $243 \times 31 \times 61$  cm was used; see figure 1 for a schematic view. The tank was filled with a homogeneous fluid layer on top of a linearly salt-stratified layer. The stratified layer was made by the two-tank method of Oster & Yamamoto (1963). First, the homogeneous layer of density  $\rho_0$  was added to the desired depth  $D$  and then the stratified layer was fed underneath, via a capped hole located at the bottom of the tank, to a depth  $L$ . After filling the tank it was left to stand for 1 hour. Care was taken to prevent a steep density jump between the homogeneous layer and the stratified layer by preparing a single stock of water for the homogeneous layer and the less-dense tank of the two-tank filling system. The tank filling was checked using the density profile obtained with a traversing conductivity probe. The stratification was repeatable within  $\pm 0.4$  kg m<sup>-3</sup> of the target salinity at the bottom of the tank.

The thermal was salt water of a density greater than the maximum stratified layer density. A cylindrical tube with a thin slot spanning the tank contained the desired thermal volume. It was pivoted on the tank walls. To generate the thermal the tube was rapidly inverted. Just prior to releasing the thermal, potassium permanganate crystals were placed on the tank floor about 5 cm to the right of the thermal impact point. The thermal on striking the bottom and on entraining the potassium permanganate became purple in colour. This served to identify the thermal fluid.

In some experiments the flow was visualized by dyeing the fluid layers, which were viewed using a shadowgraph method. To differentiate the different layers, methylene

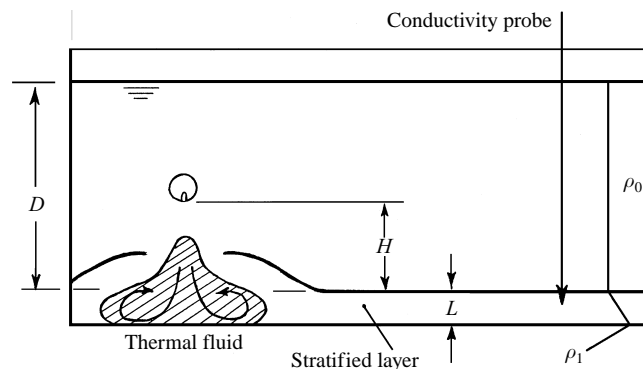


FIGURE 1. Schematic diagram of the experimental apparatus.

blue was added to the homogeneous layer, and a thin layer of fluorescein dye was introduced between the homogeneous and stratified layers.

The linearity and buoyancy frequency of the stratified layer was checked and calculated from the density profile. Speeds of propagation of the thermal and subsequent phenomena were measured *in situ* with a stopwatch and checked against the video tape measurements. The amplitude of the phenomenon was measured from the video recordings. Conductivity measurements were also taken during the experiments at a depth of 1 cm above the bottom of the tank and 80 cm from the initial thermal position. The conductivity measurements were used only as a check, since by the time the phenomenon reaches the probe its amplitude is substantially reduced.

Experiments were also performed with the system seeded by neutrally buoyant particles, in order to obtain data on the mass-transporting vertical structure by particle tracking. For these experiments, the density of the homogeneous layer was chosen to ensure that the particles (specific gravity  $\sim 1.04$  and diameter 1.08–1.46 mm) resided in the stratified layer. The DigImage software package was used to obtain data on the particle locations and tracking parameters. These were processed using independent software to create particle pathlines.

### 3. Theoretical notes

#### 3.1. The wave-dynamics regime

Disturbances of wavelength  $\lambda$  propagating in a fluid layer of depth  $D$  and stratification depth  $L$  (see figure 1) can be classified into three categories (Stamp & Jacka 1995): shallow-water waves ( $\lambda/D \gg 1$ ,  $L/D = O(1)$ ), deep-water waves ( $\lambda/D \rightarrow 0$ ,  $\lambda/L \gg 1$ ) and finite-depth waves ( $L/D \ll 1$ ,  $\lambda/L \gg 1$ ). In atmospheric and oceanic flows of interest here, the wavelengths are much smaller than the total depth of fluid, but they are much longer than the thickness of the stratified layer. Hence the interest here is on deep-water waves.

The deep-water waves can be linear, weakly nonlinear or strongly nonlinear, depending on their normalized amplitude  $a/L$ . In the experiments reported here, the flows are mostly in the strongly nonlinear regime. Details of the linear and weakly nonlinear theories have been given elsewhere (Benjamin 1967; Davis & Acrivos 1967) and these theories were placed in an atmospheric context by Rottman & Einaudi (1993) and Manasseh & Middleton (1995).

The buoyancy frequency of the lower layer,  $N^2(z)$ , is given by

$$N^2(z) = -\frac{g}{L} \frac{1}{\rho} \frac{d\rho}{dz}, \quad (1)$$

where  $\rho$  is the hydrostatic density. For the experiments considered here, the stratification is linear, so  $N$  is a constant. This also means that there is a straightforward solution to the linear and weakly nonlinear equations of motion. This gives the propagation speed of the disturbance,  $c$ , for boundary conditions of a thin stratified layer underlying a deep neutrally stratified layer (appropriate to the BDO equation) as

$$c = c_0 + \bar{a}c_1, \quad (2)$$

where  $\bar{a}$  is the maximum vertical streamline displacement  $a$ , non-dimensionalized by  $L$ , and the linear eigenvalue or wave speed is given by

$$c_0 = \frac{2NL}{(2n-1)\pi}, \quad n \in \{1, 2, 3, \dots\}, \quad (3)$$

for the  $n$ th mode. If rigid-lid (KdV-equation) boundary conditions are used,  $c_0$  is given by

$$c_0 = \frac{NL}{n\pi}. \quad (4)$$

Equation (2) is plotted in figure 6, which will be described in §4.1. It is expected that linear or weakly nonlinear theories would be of limited relevance here; as noted in §1.2, they cannot predict mass transport. However it is important to note the wave speeds linear or weakly nonlinear theories predict. Some recent fully nonlinear theories are those of Pullin & Grimshaw (1988), Forbes & Belward (1996) and Evans & Ford (1996), and numerical calculations include those of Tung *et al.* (1982) and Brown & Christie (1994).

### 3.2. Dimensional analyses

For the system described in figure 1, the important governing parameters are  $Q_0$ ,  $H$ ,  $L$ ,  $x$ , and  $N$ . Here, the total buoyancy of the thermal,  $Q_0$ , is given by  $\delta b_0 V_0$  (Noh *et al.* 1992), where  $V_0$  is the initial volume of thermal fluid per unit length, and the initial buoyancy deficit is  $\delta b_0 = g(\rho_t - \rho_0)/\rho_0$ ,  $\rho_t$  being the density of the thermal fluid and  $\rho_0$  the density of the upper (homogeneous) layer. Given typical average measured speeds and lengthscales, the Reynolds number for the horizontal component of flow is about 2000. The Reynolds number decreased with the evolution of the flow; hence viscous bottom-frictional effects are expected to dominate the horizontal propagation only at large  $x$ . The depth  $D$  of the upper layer has not been considered a parameter in view of the assumption  $L/D \ll 1$ . It will be confirmed in §4.1 that  $D$  is not a factor in the system. Also note that  $Q_0$  effectively has dimensions  $L^3 T^{-2}$  because two-dimensional flow is being considered.

For simplicity, consider the horizontal speed of propagation  $c$  of the disturbance, which should depend on  $Q_0$ ,  $x$ ,  $H$ ,  $L$  and  $N$ . The analysis is restricted to averages over a specific region of  $x$ . Then  $c$  can be written as

$$c = c(H, L, N, Q_0). \quad (5)$$

Since there are five variables in (5),  $c$  when non-dimensionalized will depend on two non-dimensional parameters. They are  $N^2 H^3 / Q_0$  and  $H/L$ , and their significance can be explained as follows.

Consider the density-driven fall of the thermal. The bulk of its motion, for  $H \gg L$  as is the case here, occurs in homogeneous fluid. Thus its speed on impacting the stratified layer scales as  $(Q_0/H)^{1/2}$  (Noh *et al.* 1992), and its length scale  $l_H$  is proportional to  $H$ . (The constant of proportionality is about 0.6.) After impact the thermal mass must deflect horizontally, splitting into a pair of opposite-travelling vortices. Experiments on descending line thermals show that these vortices are initially driven by the change in momentum imparted by the impact. However, after travelling a distance of about  $1.5l_H$  the motion is once more density-driven. Both momentum and density-driven motions still scale with  $(Q_0/H)^{1/2}$ .

Since the lengthscale of the thermal on impact is  $l_H \sim H$ , the largest possible speed scale of any internal wave motions generated on impact is  $NH$ . The ratio of this to the density-driven speed scale  $(Q_0/H)^{1/2}$  gives the parameter  $N^2H^3/Q_0$ . When  $N^2H^3/Q_0$  is very small, even the largest wave motion is much smaller than density-driven effects. Meanwhile, the parameter  $H/L$  could represent the initial potential energy of the thermal, relative to that of the stratified layer disturbed by a mass with the same buoyancy deficit.

We will now non-dimensionalize  $c$  using physical reasoning, firstly assuming the flow has aspects of density-driven behaviour, and secondly assuming it is wave dominated.

For the density-driven regime and also the transitional regime, in which density-driven effects continue to play a role, the propagation speed  $c$  should scale with  $(Q_0/H)^{1/2}$ . Therefore an appropriate non-dimensionalization for both density-driven and transitional regimes is

$$\frac{c}{(Q_0/H)^{1/2}} = f_1 \left( \frac{H}{L}, \frac{N^2H^3}{Q_0} \right), \quad (6)$$

where  $f_1, f_2, \dots$  are functions.

Eventually, the flow is expected to be dominated by the wave mechanics of the stratified layer. Now, following (3) and (4), the propagation speed should scale with  $NL$ . An appropriate non-dimensionalization is

$$\frac{c}{NL} = f_2 \left( \frac{H}{L}, \frac{N^2H^3}{Q_0} \right). \quad (7)$$

The scalings (6) and (7) will be used to interpret experimental results.

## 4. Results

### 4.1. General evolution of the phenomenon, speed and amplitude

Initial trials were undertaken to optimize the system. The intent was to maximize the physical amplitude of the phenomenon, in order to facilitate observations of its vertical structure, in particular, the mass-transporting part. This meant maximizing the stratified layer depth  $L$ ; however, if  $L$  was too large, significant wave motion did not occur, because a given impact applied to the layer resulted in a smaller amplitude when scaled by  $L$ . Attempts to create larger impacts by releasing larger thermal volumes resulted in excessive mixing. The ratio  $L/D$  had to be minimized, where  $D$  is the depth of the upper layer; if  $L/D$  was too large, the system was tending to a regime governed by the 'rigid-lid' boundary condition (4), which is less desirable since it has limited relevance to the atmospheric application. The upper layer depth  $D$  was limited by practical considerations: if  $D$  was too large, the Perspex tank walls had substantial deflections at the mid-levels, introducing optical distortion.

---

Experiment number	$H$ (cm)	$\rho_1$ (kg m <sup>-3</sup> )	$\rho_t$ (kg m <sup>-3</sup> )	$V_0$ (ml)
1.131	5.0 ± 0.2	1004.1 ± 0.4	1073.9 ± 0.4	22 ± 1
1.240	5.0 ± 0.2	1008.9 ± 0.4	1120.0 ± 1.0	22 ± 1
1.330	10.0 ± 0.2	1002.7 ± 0.4	1107.5 ± 0.3	22 ± 1
4.150	3.5 ± 0.2	1003.4 ± 0.3	1160.0 ± 0.3	22 ± 1
Minimum	2.0 ± 0.2	1002.5 ± 0.5	1020.0 ± 1.0	30 ± 1
Maximum	10.0 ± 0.2	1012.1 ± 0.4	1200.0 ± 1.0	9 ± 1

---

TABLE 1. Typical initial parameters for some experiments, together with maximum and minimum values tried for each parameter.  $H$  is defined in figure 1;  $\rho_1$ , density of the bottom of the stratified layer (the homogeneous layer had density 1000 kg m<sup>-3</sup> for dye experiments);  $\rho_t$ , density of the thermal. Variations in error bounds were caused by unavoidable variations in experiment preparation methods.

---

The optimal stratified layer depth  $L$  of 2 cm was used in all experiments. For consistency with the analysis in §3.1,  $L$  is used as a general lengthscale, and dimensionless distances quoted below are non-dimensionalized with  $L$ . The optimal value of  $D$  was 20 cm; however, as a check experiments were also run with  $D = 40$  cm, as will be described shortly. Typical values of the parameters for some experiments are given in table 1, together with maximum and minimum ranges.

Schematic drawings of typical stages in the flow evolution are given in figure 2. By the time the thermal reaches the top of the stratified layer it has entrained sufficient fluid to have expanded to a diameter several times the stratified-layer thickness. The height of the thermal vortices after impact depends on  $H/L$ ; typically the thermal-vortex height is 3–4 times the layer depth for  $H/L = 2.5$ , for example. The thermal forms a roll vortex on either side of the impact centreline. Up to about  $x = 5$ –10 non-dimensional units (10–20 cm), its behaviour appears essentially as any of the several well-documented cases of a vortex pair or vortex ring impacting a solid boundary. Examples include the work of Linden & Simpson (1985), Lundgren, Yao & Mansour (1992) and Orlandi & Verzicco (1993). The flow in the thermal vortex is turbulent, but the lengthscales of motions within the thermal appear small relative to the thermal vortex, about 1/5 its size or less. This stage is shown in figure 3(a), in which the vortices are unclear but the typical scale of the thermal impact can be seen. It is also shown diagrammatically in figure 2(a).

For some combinations of parameters, chiefly for low  $Q_0$  and strong  $N$ , the thermal vortex quickly collapses and forms a weak intrusion that only travels to  $x = 20$  or so. No waves are visible on the stratified layer. Significant motions cease quickly.

For many regions of parameter space, however, the thermal mass travels to  $x = 40$  or beyond, enclosed in a solitary ‘hump’ of stratified-layer fluid, as illustrated in figures 2(c) and 2(d) and figures 3(c) and 3(d), where the thermal mass appears purple. The length of the ‘hump’ is typically about 5 times the layer depth. This phenomenon represents the transition from a density-driven to a wave-dominated flow. It will be called an ‘isolated propagating flow’ (IPF) and its evolution is as follows.

By the time the IPF reaches about  $x = 10$ –15, the thermal mass within it has flattened out and taken a more elliptical shape, still clearly rotating in the same sense as the original thermal vortex at the impact. The stratified-layer fluid, which had been thrown up above the thermal vortex, now covers the thermal mass. Dye distributions

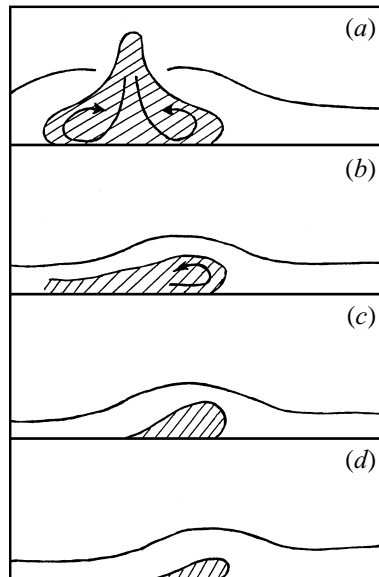


FIGURE 2. Typical stages in the flow evolution. See text for explanations.

show that the stratified-layer fluid remains quite distinct from the thermal mass. This stage is illustrated in figure 2(b). For low- $Q_0$  cases, Kelvin-Helmholtz billows can occur on the interface between the thermal fluid and the stratified-layer fluid; however, apart from these cases, no mixing of the thermal fluid and enveloping stratified-layer fluid can be observed. Figure 3(b) shows some billows above the thermal mass. A thin trail of thermal fluid leaks out along the floor from the rear of the IPF. Apart from this trail, the thermal mass is encapsulated within the IPF and moves with it, as illustrated in figures 2(c) and 3(c). The leakage of fluid in the trail is consistent with the field observations of Doviak & Ge (1984), as interpreted by Doviak *et al.* (1991). Similar leakage was also observed by Maxworthy (1980) in the laboratory.

By about  $x = 20$ – $30$ , a reduction of the size of the thermal mass inside the IPF can be observed, owing to the loss of mass to the trail behind the IPF. However, while the amplitude of the IPF does reduce throughout this time, the loss in IPF amplitude is not as great as the reduction in its encapsulated thermal mass. This will be discussed in §5. The thermal mass appears in shadowgraph visualizations to be mixed, but by this stage turbulent motions within it seem to have substantially ceased. The fluid in the thermal mass appears virtually motionless on a frame of reference moving with the IPF and does not possess any discernible net circulation or relative vorticity. This stage is shown in figures 3(c) and 3(d) and diagrammatically in figure 2(d). Transport of substantial mass in the IPF occurs over a distance typically 10 times the horizontal length scale of the IPF. Small-amplitude waves should only transport substantial mass at their propagation speeds over scales comparable with one wavelength.

Eventually the thermal mass will disappear entirely, although the time at which this occurs depends on the parameters. When this occurs, the IPF has degenerated to a phenomenon that could be described as a weakly nonlinear small-amplitude solitary wave. It will continue to propagate until it is reflected from the tank endwalls.

In general, the speed of the phenomenon decreases as it travels; in the following, the average speed over the first 40 non-dimensional units in  $x$  (80 cm) will be used.

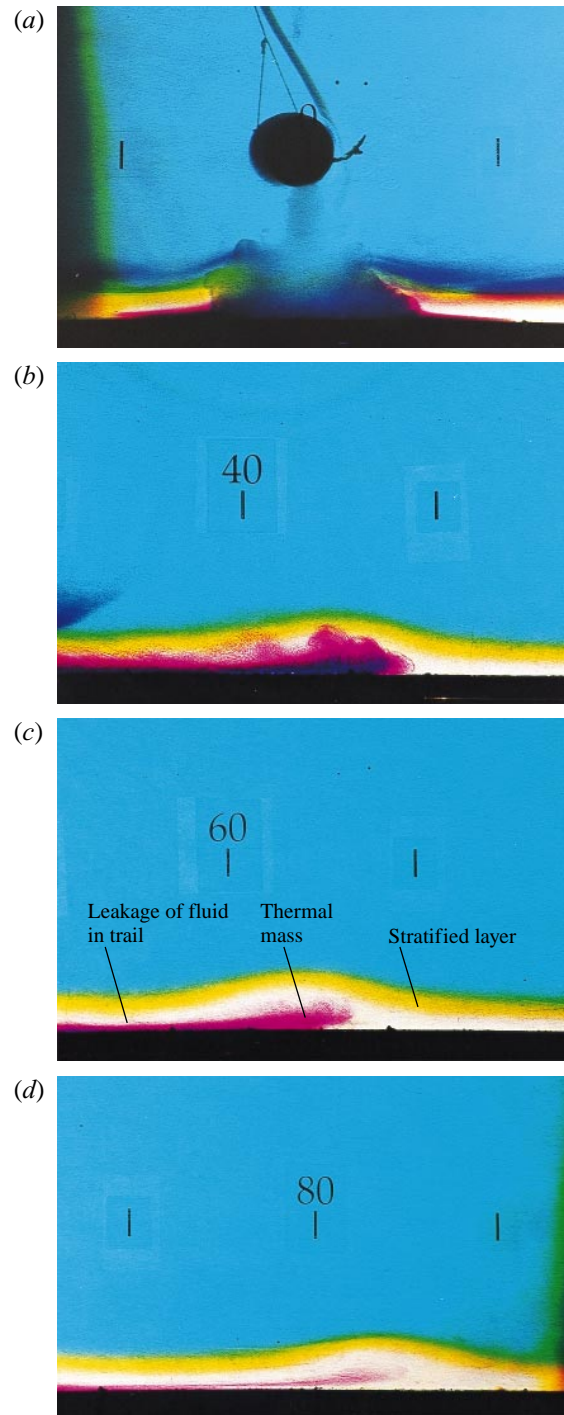


FIGURE 3. Dye visualization of a typical experiment. The marks are in cm and at every 10 cm from the centreline of the thermal origin. The homogeneous fluid is uppermost and coloured. The thermal mass has the darkest dye.  $H/L = 2.5$ ;  $N = 1.15 \pm 0.15 \text{ s}^{-1}$ ;  $\rho_i = 1197 \pm 1 \text{ kg m}^{-3}$ . The average speed over these exposures is about  $1.6 \text{ cm s}^{-1}$ . Key features of an isolated propagating flow are annotated on (c).

The averaging distance is governed by the length of the tank. This averaging removes the  $x$ -dependence in the data, allowing comparison with (7) and (6). Averaging was also attempted over shorter, consecutive intervals. However, measurements were not sufficiently accurate to clarify the functional form of the evolution of speed with distance. In some instances, the reduction of speed was not monotonic – it seemed to decrease, increase slightly, then decrease further.

For initial thermal buoyancies sufficient to generate a wave or IPF, the average propagation speeds were all in the range 1.4–2.5 cm s<sup>-1</sup>. The linear wave speed  $c_0$  given by (3) for BDO (deep-water) boundary conditions is typically 1.5 cm s<sup>-1</sup> while KdV (rigid-lid) boundary conditions give one-half of this or 0.75 cm s<sup>-1</sup>. Hence KdV boundary conditions are much less appropriate than the deep-water BDO conditions. This is seen as partial confirmation that the upper-layer depth of 10 non-dimensional units (20 cm) was adequate to place the experiments in the deep-water regime. As an additional check, a set of experiments was repeated with a non-dimensional upper-layer depth of 20 (40 cm). These data match the results with an upper-layer depth of 10, as shown on figure 4, which will be discussed next. This is consistent with Tung *et al.* (1982) who found that numerical results became similar for dimensionless depths greater than 10. Thus the results are applicable to processes in the oceanic thermocline or in the lower atmosphere that are generated by isolated dense fluid masses.

As noted in §3.2, dimensional analysis based on the observed propagation speed is a way of interpreting the flow evolution. A plot of  $c/(NL)$  versus  $N^2H^3/Q_0$  is shown in figure 4, consistent with (7). Error bars for the data are calculated using the formulae described in Moffat (1988). The data shown are the average speed over the first 40 units (80 cm).

Several features are clear from figure 4. Firstly, the speed of the disturbance does not collapse with the scaling based on the linear long-wave speed,  $NL$ . The results lie either above or below the first-mode linear long-wave speed  $c_0$  calculated using (3), which is shown in non-dimensional form by the dashed line. These observations can be attributed to the formation of solitary waves, which would increase  $c$  above  $c_0$ , or to density-driven or bottom-frictional effects, which may decrease  $c$ .

Secondly, the data indicate a substantial dependence on  $H/L$  or other factors. (The thermal release cylinder was not properly levelled for some  $H/L = 3.75$  runs, resulting in the  $H/L = 3.70$  data.) Thirdly, for a given  $H/L$ ,  $c/(NL)$  generally decreases with  $N^2H^3/Q_0$ , indicating that  $c$  decreases with decreasing energy input to the system, that is, with decreasing total buoyancy supplied,  $Q_0$ . In all, figure 4 demonstrates that  $c/(NL)$  depends on both  $H/L$  and  $N^2H^3/Q_0$ , but it fails to illustrate the existence of the regime in which transitions from density-driven to wave-dominated behaviour occur.

Figure 5 illustrates relationship (6). It scales  $c$  by the thermal arrival speed at the top of the stratified layer ( $\sim (Q_0/H)^{1/2}$ ). It is evident that below a certain critical value of  $N^2H^3/Q_0$  (about 50 to 80)  $c^2H/Q_0$  is independent of  $H/L$ , since data from experiments at quite different  $H/L$  collapse onto the same curve. However, figure 5 shows that the flow is strongly dependent on  $N^2H^3/Q_0$ , so that stratification plays a key role. It is also striking that it is only below this critical value that the IPF was observed. The experiments beyond the critical value of  $N^2H^3/Q_0$  resulted in a wave travelling ahead of the thermal mass, rather than a transitional regime between density-driven and wave-dominated flows. Thus, the condition for the formation of an IPF may be stated as  $N^2H^3/Q_0 < 50$  to 80. In this IPF regime the average disturbance speed is independent of  $H/L$ .

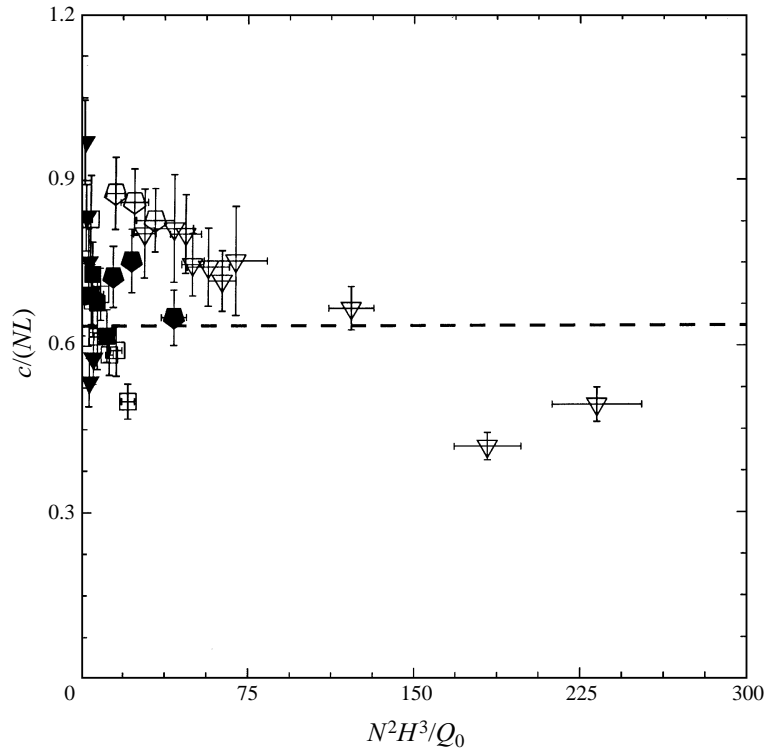


FIGURE 4. Scaling for wave-dominated physics. Non-dimensional propagation speed  $c/(NL)$  from  $x = 0$  to  $x = 40$  (80 cm), versus the parameter  $N^2 H^3 / Q_0$ . The dashed line is the first-mode linear wave speed corresponding to BDO boundary conditions. The thermal release cylinder was not perfectly level for  $H/L = 3.70$  runs. ■:  $D/L = 20$ ,  $H/L = 2.5$ ; □:  $D/L = 10$ ,  $H/L = 2.5$ ; and for  $D/L = 10$ , ▽:  $H/L = 5.0$ ; ○:  $H/L = 3.70$ ; ●:  $H/L = 3.75$ ; ▼:  $H/L = 1.75$ .

Measurements were also made of the amplitude of the phenomenon, from the video record. Measurements were made at 10 cm intervals starting at 20 cm, i.e. at  $x = 10, 15, 20, 25, 30, 35$  and 40. Amplitude was defined as the maximum displacement of the top of the stratified layer above the undisturbed layer height in front of the phenomenon. Also, the ‘incremental speeds’ were measured: these were calculated from the time taken to cover each interval of 5 units in  $x$ . Owing to large scatter in the data, averaging was necessary. The data were averaged for each  $H/L$  value. The result is presented in figure 6, along with the relationship between wave speed and amplitude predicted by the weakly nonlinear theory described by (2). Since the average data inevitably incorporates the density-driven, IPF and weakly nonlinear wave regimes, it was not possible to make a direct comparison with weakly nonlinear wave theory.

Weakly nonlinear theory can only reasonably be applied while the small parameter  $\bar{a} = a/L$  used in its derivation remains ‘small’, up to possibly 0.5 (Tung *et al.* 1982), but certainly no greater than 1.0. The results here are beyond the regime where weakly nonlinear theory is probably valid. Uncertainty in the amplitude measurements contributes to the significant scatter, despite averaging. The practical difficulty in producing thermal-generated laboratory IPFs with large and controllable amplitude prevented a large amplitude range from being systematically explored, as Stamp & Jacka (1995) did. Nevertheless, the results indicate that a simple relationship

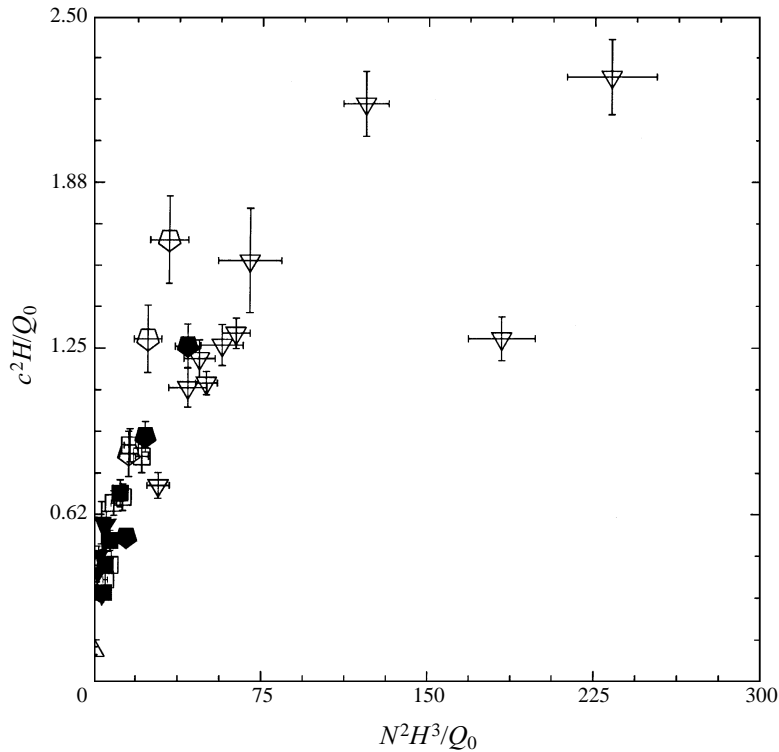


FIGURE 5. Scaling for density-driven and transitional physics. Non-dimensional propagation speed  $c^2H/Q_0$  from  $x = 0$  to  $x = 40$  (80 cm), versus the parameter  $N^2H^3/Q_0$ ;  $D/L = 10.0$  for all points. Symbols as figure 4.

between speed and amplitude, such as that expected on the basis of weakly nonlinear wave theory, cannot be the only factor affecting the results. The ‘wavelength’ of the phenomenon was also measured, and, while similarly scattered, shows a broad trend of increasing with amplitude.

#### 4.2. Vertical structure of the phenomenon – mass transport

The camera was placed at different positions downstream of the release point and the experiment repeated with identical parameters at each position. After a few trials the flows at each position seemed perfectly repeatable. For the particular study to be described below, the parameter  $N^2H^3/Q_0$  was 5.5. This well below the critical value suggested by the results of §4.1, hence an IPF was generated. The parameter  $H/L$  was 2.5. The flow evolution revealed by these studies is as follows.

In the first stage, particles in the stratified layer are caught up in the thermal vortex. This stage is shown in figure 7. The data shown covers 30 s. Solid lines join the particle images belonging to the same particle. The wave is travelling from left to right across the frame and those particles in orbital paths are rotating counter-clockwise. The dominant motion is the positive-vorticity (counter-clockwise in figure 7) circulation of the thermal vortex. Particles follow smooth curved paths when caught up in this vortex. The equivalent stage is shown in figure 2(a) and figure 3(a).

Subsequently, the flow begins to translate to the right. Particles are clearly moved right across the image frame. There is still a strong positive vorticity throughout the flow region.

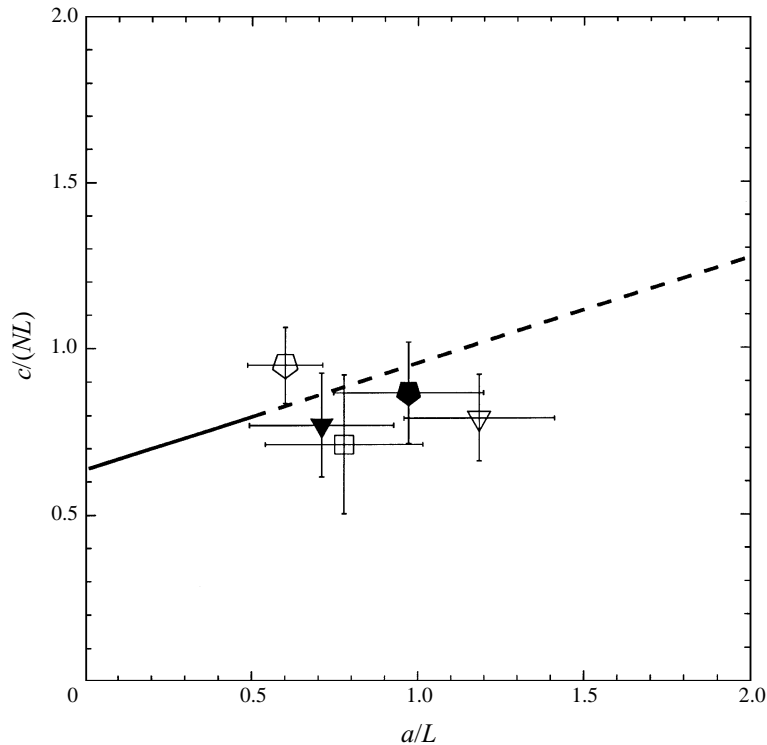


FIGURE 6. Speed of the phenomenon versus amplitude. These are averages of the incremental speeds over all experiments for each  $H/L$  value. Symbols as figure 4; data for  $D/L = 10$  and  $D/L = 20$  are combined. Error bars are calculated as pooled standard deviations. The solid line up to  $a/L = 0.5$  is the relationship predicted by weakly nonlinear theory for a first-vertical-mode soliton; the dashed line is the extrapolation of this relationship beyond the regime where weakly nonlinear theory should be valid. The first-mode linear speed is at  $a/L = 0$ .

By about  $x = 20$ , the flow is in the transitional or IPF regime. This is illustrated in figure 8. This equivalent stage is shown in figure 2(d) and figures 3(c) and 3(d). The IPF appears to have a dual structure, consisting of a zone of translating mass in the lower portion and a zone of wave activity in the upper portion. The two zones are clearly distinguishable because in the mass-transport zone particles are moved horizontally across the frame with relatively little vertical motion, whilst in the wave-activity zone particles travel on elliptical orbits with no substantial net translation. By 'no substantial' it is meant that after completing the orbit the particle's position appears to be the same as before its motion began. Furthermore, in the mass-transport zone there seems to be virtually no shear or net circulation. This is consistent with the observation noted in §4.1 above, where the dyed thermal mass appeared to be virtually motionless in a frame moving with the IPF. Note that in figure 8 the curved paths in the top zone represent particles travelling on the elliptical orbits typical of wave flows; they do not appear to have been caught up in turbulent eddies, and no significant turbulence was noted in the shadowgraph experiments for these parameters. Eddies associated with gravity-current motion should show some net translation, whereas these motions do not. The sense of rotation of the particles on their orbits is counter-clockwise, which is the same as the positive vorticity initially created by the thermal vortex. These orbits only exist in the wave-activity zone. The thermal-vortex structure apparently facilitates the formation of wave-dynamical particle orbits.

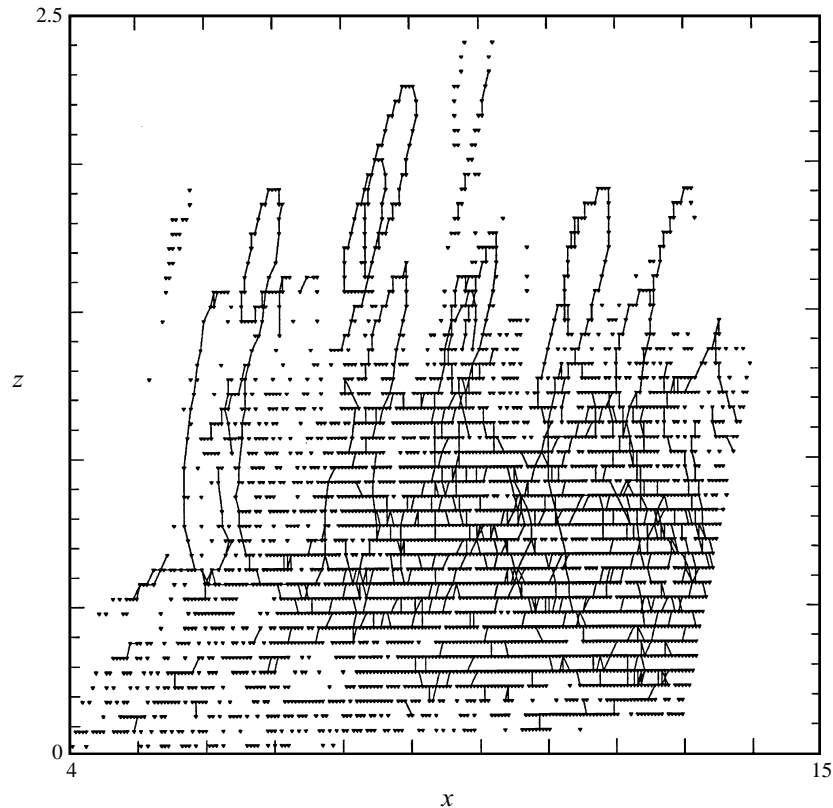


FIGURE 7. Particle tracks in the density-driven regime. The centre of the frame is at  $x = 9.5 \pm 0.1$ . Each dot represents a particle at 0.2 s intervals. The dimensions of the region shown are 11.0 in  $x$  and 2.5 in  $z$  (22.0 by 5.0 cm). Thirty seconds' data are shown on this frame, beginning immediately after thermal release. Solid lines join the particle images that particle-tracking algorithms confirm as belonging to the same particle. Groups of particles appear to be organized into horizontal bands because the aspect ratio of the plot, chosen to emphasize the vertical structure, magnifies the pixel resolution in the vertical. The wave is travelling from left to right across the frame and those particles in orbital paths are rotating counter-clockwise.

The next stage in flow evolution occurs when significant transport of particles ceases. This point is hard to determine precisely from the particle tracking measurements but occurs after about  $x = 30$ . The IPF now appears to have been replaced by a solitary wave that does not transport mass. The behaviour appears wave-dynamical throughout the vertical structure.

Finally, the vertical structure after the IPF has degenerated consists of a smoothly varying and essentially horizontal velocity that is a maximum near the floor and decreases with height through the stratified layer. This is the basic vertical structure predicted by the first-vertical-mode ( $n = 1$ ) linear solution corresponding to (3). The weakly nonlinear analysis separates the streamfunction into vertical and horizontal functions; the vertical eigenfunctions are obtained in the same way as for the linear analysis. Therefore, flows consistent with weakly nonlinear solutions should have the same vertical structure as the linear solution. The sense of vorticity observed from the shear in the flow is still positive.

The speed of the IPF for the conditions of figure 8, obtained from an average of sev-

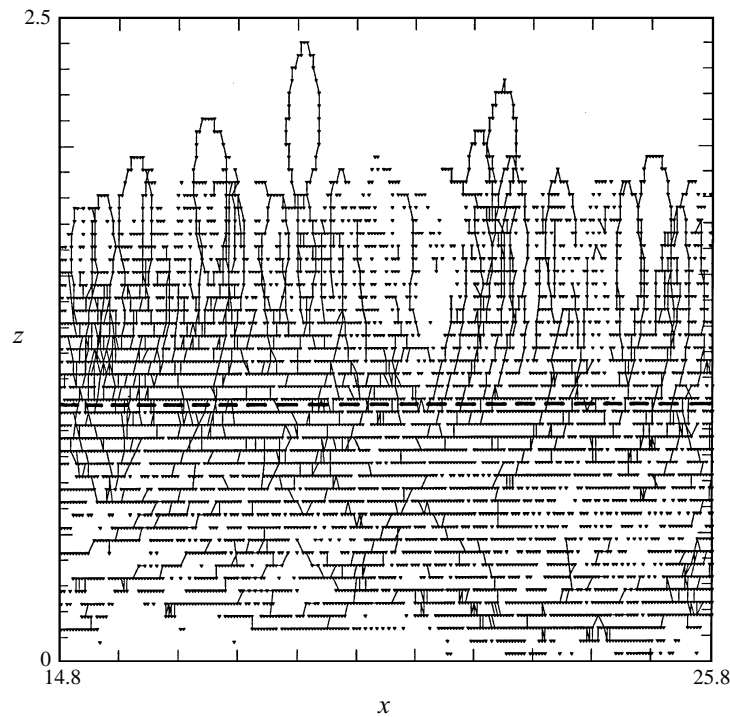


FIGURE 8. Particle tracks in the transitional stage of flow evolution, corresponding to an IPF. The centre of the frame is at  $x = 20.3 \pm 0.1$ . The wave-activity zone is above about  $z = 1.0$  (the thick dashed line) and the mass-transport zone is below. This stage corresponds to figure 2(d), in which the transported mass is hatched. Other details as figure 7.

eral repeated runs, was estimated at  $1.06 \pm 0.3$ , scaled relative to  $c_0$ , or  $1.63 \pm 0.4 \text{ cm s}^{-1}$  in dimensional units. This speed is subtracted from the horizontal component of the particle velocities to give a pathline pattern in a frame of reference moving with the IPF. This is shown in figure 9. Pathlines are not the same as streamlines unless the flow is steady. While the flow at the stage of figure 9 is non-turbulent, it strictly ought to be described as unsteady, since it evolves with time. Nevertheless, since major changes in the flow structure are not occurring during the time-frame represented by figure 9, there is reasonable justification for treating it as an approximate streamline pattern for the IPF.

It can be seen from figure 9 that there is a smooth symmetric pattern characteristic of soliton solutions (e.g. Benjamin 1967). The mass-transport zone appears below the crest of the wave, in the region marked 'MTZ'; it is identifiable because pathlines, as plotted in the frame of reference moving with the wave, can be observed either diverting above the mass-transport zone or stagnating at it. In this frame of reference there is no discernible motion of particles in the mass-transport zone, again confirming the visual observations in §4.1 that there seemed to be no net circulation in this zone. When the equivalent pattern for the earlier, density-dominant regime (the data of figure 7) is plotted in this fashion, it looks similar, though it is not symmetric. In the later wave-dominant regime, curvature in the streamlines is found closer to the floor. Close examination of figure 9 shows a smaller 'hump' trailing the main soliton structure, marked 'TW'. Similar trailing waves were often noticed in the density probe

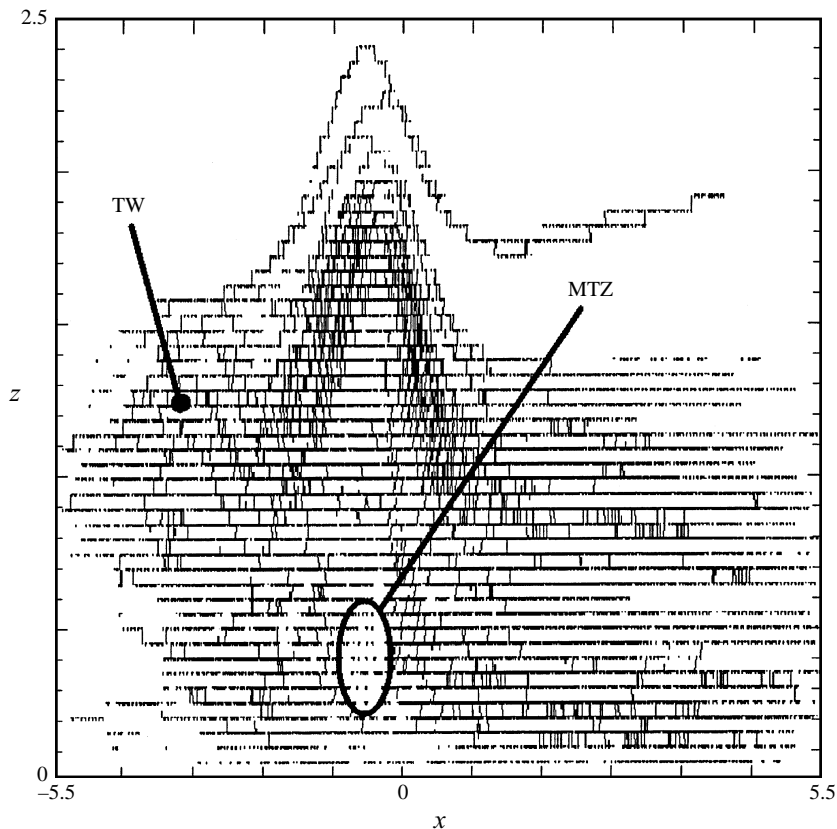


FIGURE 9. Pathline pattern of an IPF. The data are identical to that of figure 8, but plotted in a frame of reference moving with the IPF at its speed of propagation,  $1.63 \pm 0.4 \text{ cm s}^{-1}$ . The pathlines are interpreted as approximate streamlines. The particles were tracked for a greater time before the passage of the IPF than after; hence the relative displacement of the zero on the  $x$ -axis and the peak in the pattern. MTZ: the mass-transporting zone, in which particles appear quasi-stationary in this frame of reference; TW: a small trailing wave. Other details as figure 8.

traces, although they could not be seen by eye during the experiments or on the videotapes.

To make the pattern of particle tracks in figure 9 clearer, selected tracks (approximate streamlines) are shown in figure 10. The upper tracks illustrate the wave-like character of the upper wave-activity zone, including the trailing wave. The lower tracks simply stagnate at the boundary of the mass-transport zone. No evidence of recirculating flow can be discerned, however; this point will be discussed in §5 below.

## 5. Discussion

Existing theory and numerical work on strongly nonlinear waves (Tung *et al.* 1982; Brown & Christie 1994) predicts wave speed rising with amplitude faster than weakly nonlinear theory. Experiments by Stamp & Jacka (1995) agreed with these predictions. The present experiments are unable to confirm this trend, partly because of the comparatively narrow amplitude range studied, and possibly because the IPFs are sufficiently density-driven to make wave-dynamical analyses inappropriate.

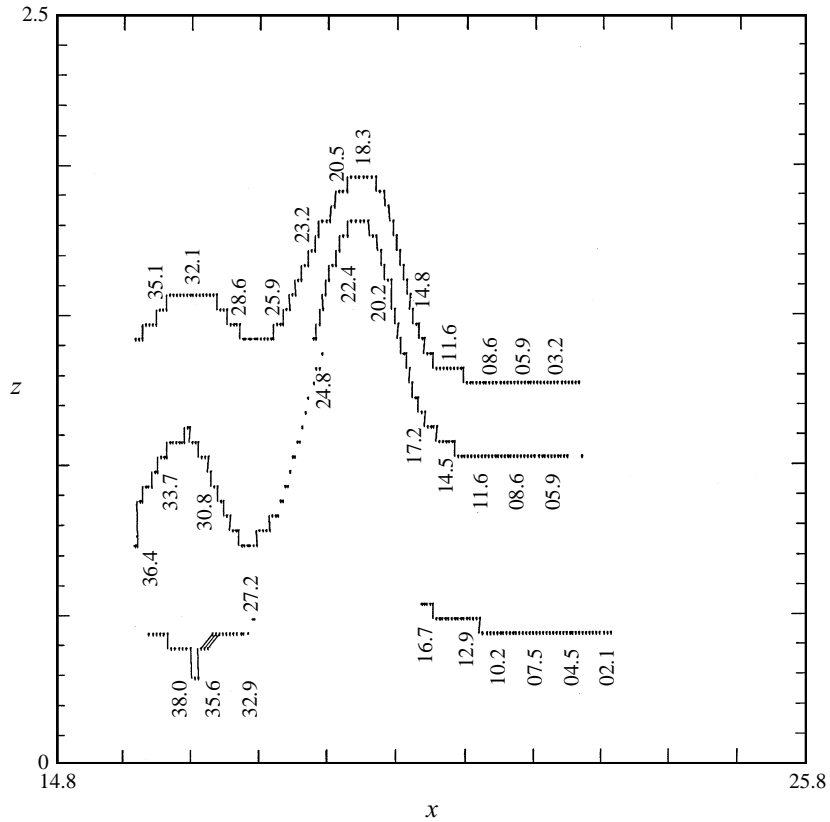


FIGURE 10. Pathline pattern of an IPF, in a frame of reference moving with the IPF at its speed of propagation,  $1.63 \pm 0.4 \text{ cm s}^{-1}$ . As figure 9, but here only selected particle tracks are shown. Time labels shown appear directly above or below the particle's location at that time. Time elapsed since thermal release is non-dimensionalized using the buoyancy frequency  $N = 1.35 \text{ s}^{-1}$ . The bottom track stagnates at the boundary of the mass-transport zone.

The dye and particle-tracking experiments show that transport of mass occurs over a distance an order of magnitude greater than the horizontal 'wavelength' of the IPF, placing it well beyond the behaviour permitted for linear or weakly nonlinear waves. This is consistent with amplitudes being generally larger than the acceptable range of validity of weakly nonlinear theory. Equally, the lack of a continuous upstream supply of dense fluid forcing the motion makes it impossible to describe the IPF as a gravity current, and the fact that fluid is lost to the trail implies that the feeder-flow structure characteristic of gravity currents (Simpson 1987) does not exist. While in many cases propagation speeds are greater than linear wave theory would predict, the IPFs studied here do not all travel faster than the linear speed, as solitary waves are expected to. (See figure 4.)

The formation of a closed streamline zone has been predicted by the numerical studies of Davis & Acrivos (1967) and by Tung *et al.* (1982) and has been associated with the mass-transporting zone observed in experiments. If the streamfunction is continuous across a closed streamline, it implies a net circulation or at least some vorticity within. However, relative motion within the mass-transporting zone was not found in the present experiments. This should not be too surprising, in hindsight, for

the above-mentioned authors note that the theoretical basis of their calculations is invalidated once closed streamlines form.

The presence of a solid boundary can change the flow structure of the present system significantly from the interfacial soliton system; Stamp & Jacka (1995) studied an interfacial soliton system and did report circulation within 'cells', although, since fluid was continually entrained into these cells and lost from them, they were not consistent with the closed-streamline regions predicted numerically by Davis & Acrivos (1967) and Tung *et al.* (1982).

It is possible that the absence of significant vorticity within the mass-transporting zone may be related to bottom friction – the boundary layer completely damping out the flow pattern that would be calculated under inviscid theory. Such calculations (Tung *et al.* 1982) were made for solitons on an interfacial layer, not at a boundary as in the present experiments. For an inviscid flow, they should be equally applicable, since the centre streamline could be replaced by a solid boundary. However, on a solid boundary there will be a viscous boundary layer. According to §4.1, turbulent motions were no longer evident by the time the IPF is formed. Thus, the influence of a turbulent boundary layer is hard to gauge, and moreover, there is no evidence of significant turbulent damping once the IPF is formed. A purely viscous (rather than turbulently eddy-viscous) boundary layer would be too small to affect flow in the closed-streamline zone. This is because, given flow speeds relative to the boundary of the order of  $1 \text{ cm s}^{-1}$ , the length scales of the viscous boundary layer would be of order tenths of a mm, compared with a closed-streamline zone that is about 1 cm in size.

One possibility is that the vorticity generated at the boundary by the initial thermal rotation is advected with the transported mass. Being of opposite sign to the rotation expected within a strongly nonlinear soliton, the advected vorticity effectively cancels it. It may be possible that an intermediate spatial zone exists, separating the lower mass-transport zone from the upper wave-dynamics zone, and that there is a net rotation of fluid in this intermediate zone. The regions which can definitely be called a wave-activity zone and definitely a mass-transport zone in figure 8 or figure 9 are not quite adjacent. This may be due to the lack of clarity in the experimental data, but it may also be due to the presence of an intermediate zone in which flow is rotating. This zone would allow a smooth matching of the vorticity gradient in the wave-dynamics zone to an apparently zero vorticity in the mass-transport zone.

The reduction with time in the amplitude of the IPF is small compared to the reduction in the size of the encapsulated thermal mass which leaks out in the trail. This may be because fluid from the stratified layer has been entrained to replace some of the lost thermal mass; alternatively, kinetic energy may have been transferred from the lost thermal mass to the wave-action zone. Christie (1989) has studied numerically the evolution of a train of solitary waves. He noted that the amplitude of the leading soliton may become exceptionally large as the evolution from initial disturbance to final state progresses. This tendency for amplitude growth may partly offset the reduction due to loss of thermal mass. A small trailing wave was noted in the present experiments, so the main IPF could be considered part of a train.

The existence of the small trailing wave behind many of the IPFs may be consistent with the theory described by Akylas & Grimshaw (1992). In their theory, oscillatory 'tails' represent a drain of energy from the main soliton. Their theory is specific to waves on a thin interface in a deep fluid, but may apply to an interfacial region in the present experiments. The loss of fluid to the thin trail behind the IPF represents a loss of momentum.

## 6. Conclusion

The impact of a descending two-dimensional thermal on a thin stratified layer overlying a solid surface leads to the formation of horizontally propagating fluid masses on the surface. In this system, there is a pair of such masses, created from each half of the thermal vortex. Each of these masses encapsulates fluid from the thermal. They travel along with solitary displacements in the isopycnals of the background stratification.

These phenomena could be called ‘isolated propagating flows’ (IPFs). They are found for  $N^2H^3/Q_0 < 50$  to 80. The IPF occurs as a density-driven flow evolves with time into a wave-dominated flow. They lack the continuous upstream supply of dense fluid and the feeder-flow internal structure characteristic of gravity currents. They transport substantial mass over a distance an order of magnitude greater than their horizontal ‘wavelength’. Hence, from the viewpoint of wave mechanics, they must be regarded as a type of strongly nonlinear solitary wave. They are of importance in understanding environmental phenomena such as wind shear due to thunderstorm outflows. They are also relevant to the generation of ‘solitary’ waves under leads in the winter polar ice, which may appear like outward ‘jet-like’ flows.

The IPF initially transports substantial mass of thermal fluid. Some leakage of this fluid always occurs, ultimately leading to a loss of the original mass of thermal fluid. The propagation speed of IPFs (averaged over  $x = 0$  to  $x = 40$ ) followed a plausible scaling for a density-driven flow, described by

$$\frac{c}{(Q_0/H)^{1/2}} = f\left(\frac{N^2H^3}{Q_0}\right), \quad (8)$$

for  $N^2H^3/Q_0 < 50$  to 80, which is independent of the second parameter  $H/L$ . Note that a wave-dominated scaling would incorporate the effect of  $L$ . However, at large  $N^2H^3/Q_0$ , this scaling based on density-driven effects breaks down. This is consistent with visual observations of those datapoints representing waves of small or negligible amplitude, rather than an IPF.

The amplitudes observed were generally beyond the range of validity of weakly nonlinear theory. IPF speeds were both above and below to the first-vertical-mode linear wave speed; most were significantly greater, but some IPFs also travelled slower than the linear speed.

The vertical structure of the observed IPFs consists of an upper zone in which the behaviour is essentially wave-dynamical, and a lower zone in which transport of mass occurs. The mass-transporting zone slowly shrinks until no significant mass transport occurs. After this stage the flow behaves essentially as a weakly nonlinear solitary wave.

The absence of significant vorticity within the mass-transporting zone, and its presence in the wave-dynamical zone, implies that a single mathematical solution may not be possible throughout the IPF. Separate analyses may be required, to be matched at the boundary between the zones. An inviscid solution for the wave-dynamical zone, matched to an interior, possibly eddy-viscous, solution may capture most of the relevant dynamics.

Stratified and rotating flow research at Arizona State University is funded by the United States Office of Naval Research (High-latitude Dynamics and Physical Oceanography) and the US National Science Foundation. We are grateful to Tia Lueck (supported by an ONR highschool traineeship) and Angelica Robles (supported by

NSF and REV awards) for help with the experiments, and to Andjelka Srdic for help with image processing. Some of the preparation of this paper was done at the School of Mathematics of the University of New South Wales and at the CSIRO Advanced Fluid Dynamics Laboratory. R.M. would like to thank the students and staff of the Mechanical and Aerospace Engineering Department at Arizona State University for making his visit pleasant and memorable. Advice from anonymous reviewers resulted in a much-improved version of the paper.

## REFERENCES

- AKYLAS, T. R. & GRIMSHAW, R. H. 1992 Solitary internal waves with oscillatory tails. *J. Fluid Mech.* **242**, 279–298.
- ALPERS, W. & STILKE, G. 1996 Observation of a nonlinear wave disturbance in the marine atmosphere by the synthetic aperture radar aboard the ERS 1 satellite. *J. Geophys. Res.* **101**, C3, 6513–6525.
- BENJAMIN, T. B. 1967 Internal waves of permanent form in fluids of great depth. *J. Fluid Mech.* **29**, 559–592.
- BENJAMIN, T. B. 1968 Gravity currents and related phenomena. *J. Fluid Mech.* **31**, 209–248.
- BRITTER, R. E. & SIMPSON, J. E. 1981 A note on the structure of an intrusive gravity current. *J. Fluid Mech.* **112**, 459–466.
- BROWN, D. J. & CHRISTIE, D. R. 1994 Fully nonlinear solitary waves in the lower atmosphere. *Proc. 6th Conf. on Mesoscale Processes, 18–22 July, Portland, Oregon, USA.*
- CHRISTIE, D. R. 1989 Long nonlinear waves in the lower atmosphere. *J. Atmos. Sci.* **46**, 1462–1491.
- CHRISTIE, D. R. 1992 The morning glory of the Gulf of Carpentaria: a paradigm for non-linear waves in the lower atmosphere. *Austral. Met. Mag.* **41**, 21–60.
- CLARKE, R. H., SMITH, R. K. & REID, R. K. 1981 The Morning Glory of the Gulf of Carpentaria: An atmospheric undular bore. *Mon. Wea. Rev.* **109**, 1726–1750.
- DAVIS, R. E. & ACRIVOS, A. 1967 Solitary internal waves in deep water. *J. Fluid Mech.* **29**, 593–607.
- DOVIK, R. J., CHEN, S. S. & CHRISTIE, D. R. 1991 A thunderstorm-generated solitary wave observation compared with theory for nonlinear waves in a sheared atmosphere. *J. Atmos. Sci.* **48**, 87–111.
- DOVIK, R. J. & CHRISTIE, D. R. 1989 Thunderstorm-generated solitary waves: a wind shear hazard. *J. Aircraft* **26**, 423–431.
- DOVIK, R. J. & GE, R. 1984 An atmospheric solitary gust observed with a Doppler radar, a tall tower and a surface network. *J. Atmos. Sci.* **41**, 2259–2573.
- EVANS, W. A. B. & FORD, M. J. 1996 An integral equation approach to internal (2-layer) solitary waves. *Phys. Fluids* **8**, 2032–2047.
- FORBES, L. K. & BELWARD, S. R. 1996 Atmospheric solitary waves: some applications to the Morning Glory of the Gulf of Carpentaria. *J. Fluid Mech.* **321**, 137–155.
- FULTON, R., ZRNIĆ, D. S. & DOVIK, R. J. 1990 Initiation of a solitary wave family in the demise of a nocturnal thunderstorm density current. *Mon. Wea. Rev.* **47**, 319–337.
- GRIMSHAW, R. H. J., HELFRICH, K. R. & WHITEHEAD, J. A. Conduit solitary waves in a visco-elastic medium. 1992 *Geophys. Astrophys. Fluid Dyn.* **65**, 127–147.
- HASSE, S. P. & SMITH, R. K. 1984 Morning glory wave clouds in Oklahoma: A case study. *Mon. Wea. Rev.* **112**, 2078–2089.
- HASSE, S. P. & SMITH, R. K. 1989 The numerical simulation of atmospheric gravity currents. Part II: Environments with stable layers. *Geophys. Astrophys. Fluid Dyn.* **46**, 35–51.
- HJELMFELT, M. R. 1988 Structure and life of microburst outflows observed in Colorado. *J. Appl. Met.* **27**, 900–927.
- LINDEN, P. F. & SIMPSON, J. E. 1985 Microbursts – a hazard for aircraft. *Nature* **317**, 601–347.
- LONG, R. R. 1953 Some aspects of the flow of stratified fluids. *Tellus* **5**, 42–58.
- LUNDGREN, T. S., YAO, J. & MANSOUR, N. N. 1992 Microburst modelling and scaling. *J. Fluid Mech.* **239**, 461–488.
- MANASSEH, R. & MIDDLETON, J. H. 1995 Boundary-layer oscillations from thunderstorms at Sydney Airport. *Mon. Wea. Rev.* **123**, 1166–1177.

- MAXWORTHY, T. 1980 On the formation of nonlinear internal waves from the gravitational collapse of mixed regions in two and three dimensions. *J. Fluid Mech.* **96**, 47–64.
- MOFFAT, R. J. 1988 Describing the uncertainties in experimental results. *Expl Thermal Fluid Sci.* **1**, 3–17.
- NOH, Y., FERNANDO, H. J. S. & CHING, C. Y. 1992 Flows induced by the impingement of a two-dimensional thermal on a density interface. *J. Phys. Oceanogr.* **22**, 1207–1220.
- NOONAN, J. A. & SMITH, R. K. 1985 Linear and weakly nonlinear internal wave theories applied to “Morning Glory” waves. *Geophys. Astrophys. Fluid Dyn.* **33**, 123–143.
- ONO, H. 1975 Algebraic solitary waves in stratified fluids. *Tellus* **5**, 42–58.
- ORLANDI, P. & VERZICCO, P. 1993 Vortex rings impinging on walls: axisymmetric and three-dimensional simulations. *J. Fluid Mech.* **256**, 615–646.
- OSTER, G. & YAMAMOTO, M. 1963 Density gradient techniques. *Chem. Rev.* **63**, 257–268.
- PULLIN, D. I. & GRIMSHAW, R. H. J. 1988 Finite-amplitude solitary waves at the interface between two homogeneous fluids. *Phys. Fluids* **31**, 3550–3559.
- ROTTMAN, J. W. & EINAUDI, F. 1993 Solitary waves in the atmosphere. *J. Atmos. Sci.* **50**, 2116–2136.
- ROTTMAN, J. W. & SIMPSON, J. E. 1989 The formation of internal bores in the atmosphere: a laboratory model. *Q. J. R. Met. Soc.* **115**, 941–963.
- SCORER, R. S. 1958 *Natural Aerodynamics*. Pergamon.
- SHREFFLER, J. H. & BINKOWSKI, F. S. 1981 Observations of pressure jump lines in the Midwest, 10–12 August 1976. *Mon. Wea. Rev.* **109**, 1713–1725.
- SIMPSON, J. E. 1987 *Gravity Currents: In the environment and the Laboratory*. Ellis Horwood.
- STAMP, A. & JACKA, M. 1995 Deep-water internal solitary waves. *J. Fluid Mech.* **305**, 347–371.
- TUNG, K. K., CHAN, T. F. & KUBOTA, T. 1982 Large amplitude internal waves of permanent form. *Stud. Appl. Maths*, **66**, 1–44.
- TURNER, J. S. 1963 The motion of buoyant elements in turbulent surroundings. *J. Fluid Mech.* **16**, 1–16.